

# We are IntechOpen, the world's leading publisher of Open Access books Built by scientists, for scientists

6,900

Open access books available

186,000

International authors and editors

200M

Downloads

Our authors are among the

154

Countries delivered to

TOP 1%

most cited scientists

12.2%

Contributors from top 500 universities



WEB OF SCIENCE™

Selection of our books indexed in the Book Citation Index  
in Web of Science™ Core Collection (BKCI)

Interested in publishing with us?  
Contact [book.department@intechopen.com](mailto:book.department@intechopen.com)

Numbers displayed above are based on latest data collected.  
For more information visit [www.intechopen.com](http://www.intechopen.com)



# Analysis and Design of Radome in Millimeter Wave Band

Hongfu Meng and Wenbin Dou

*State Key Laboratory of Millimeter Waves, Southeast University, China*

## 1. Introduction

Antenna is a very important component in a radar system. In order to protect the antenna from various environments, dielectric radome is always covered in front of the antenna. However, the presence of the radome inevitably affects the radiation properties of the enclosed antenna, such as loss and distortion of the radiation pattern. For the monopulse tracing radar, the appearance of the radome will deviate the null direction of the difference radiation pattern from the look angle of the antenna, which is called the boresight error (BSE) of the radome. Thus, an accurate analysis of the antenna-radome system is very important.

As the wavelength of the millimeter wave is shorter than microwave, the millimeter wave radar is more and more popular in monopulse radar system to improve the tracing precision. However, as the size of the radome in millimeter wave band is always tens of wavelengths or larger, the full-wave methods, such as the method of moments (MoM) [Arvas et al, 1990] and the finite element method (FEM) [Gordon & Mittra, 1993], are very difficult to be implemented. Whereas, the high-frequency methods [Gao & Felsen, 1985; Paris, 1970], e.g., the aperture integration-surface integration (AI-SI) method [Paris, 1970; Volakis & Shifflett, 1997], are very efficient and can provide an acceptable solution for the radome with smooth surface. But for the tangent ogive radome, as there is a nose tip in the front of the radome, the AI-SI method is also not suitable and can not get the accurate results.

In 2001, the hybrid physical optics-method of moments (PO-MoM) was proposed to analyze the radome with nose tip [Abdel et al., 2001]. In the hybrid method, the radome was divided into two parts: the high frequency part with the smooth surface and the low frequency part with the tip nose region. The high frequency part was analyzed by the high frequency method, such as the AI-SI method. Then, the surface integration equation was established on the radome surface, and the equivalent currents on the high frequency part of the radome were substituted into the equation to reduce the unknowns. Finally, the equation with the unknowns in the low frequency region was solved to obtain the surface currents on the radome. However, for the radome with some complex small structures, such as the multilayer radome or the radome with the metallic cap, this hybrid method is very difficult. So some new hybrid methods must be proposed to solve these problems.

The aim of antenna-radome analysis is to improve the performance of the radar system. So, the optimal design of the antenna-radome system is very necessary. During the last two decades,

many researches have been done to optimize the antenna-radome system. Hsu, et al. optimized the BSE of a single-layered radome using simulated annealing technique in 2D [Hsu et al., 1993] and 3D [Hsu et al., 1994] with variable thickness radome. The polarization and frequency bandwidth performances of a C-sandwich uniform thickness radome have been optimized in [Fu et al., 2005] using the genetic algorithm (GA). The power transmission property and BSE of a variable thickness A-sandwich radome have also been compromised between two uniform thickness radomes [Nair & Jha, 2007].

As there are few literatures to discuss about the radome in millimeter wave band, in this chapter, we mainly focus on the analysis and optimal design of the radome in millimeter wave band. This chapter is divided into the following three parts.

In section 2, we discuss about the high frequency method for the radome analysis. Firstly, the general steps of the AI-SI method to analyze the electrically large radome are given. Then, the transmission coefficient in the case when the wave is passing through the radome is derived from the transmission line analogy. As the incident angles of the millimeter wave antenna-radome system are always very large and the electrical thickness of the radome is large, the traditional AI-SI method, which is very popular in microwave band, must be modified to analyze the radome in millimeter wave band. So, a phase factor of the lateral transmission is deduced to modify the conventional transmission coefficient. With this modified transmission coefficient, a conical radome at W-band is analyzed by the AI-SI method, and the computational and experimental results are compared.

To analyze the radome with some small complex structures, we present a hybrid method that combines high frequency (HF) and boundary integral-finite element method (BI-FEM) together in section 3. The complex structures and their near regions (LF part) are simulated using BI-FEM, and the other flat smooth sections of the radome (HF part) are modeled by the AI-SI method. The fields radiated from the equivalent currents of the HF part determined by the AI-SI method are coupled into the BI-FEM equation of the LF part to realize the hybridization. In order to account for the higher-order interactions of the radome, the present hybrid method is used iteratively to further improve the accuracy of the radome analysis. Also, some numerical results are given to show the validation of the hybrid method.

In the last section of this chapter, in order to optimize the radome in millimeter wave band, we employ GA combined with the ray tracing (RT) method to optimize the BSE and power transmittance of an A-sandwich radome in millimeter wave band simultaneously. In the optimization process, the RT method is adopted to evaluate the performances of the desired radome, and GA is employed to find the optimal thickness profile of the radome that has the minimal BSE and maximal power transmittance. In order to alleviate the difficulties of the manufacture, a new structure of local uniform thickness is proposed for the radome optimization. The thickness of the presented radome keeps being uniform in three local regions and only varies in two very small transitional regions, which are more convenient to be fabricated than the variable thickness radome [Hsu et al., 1994; Fu et al., 2005; Nair & Jha, 2007].

## **2. High Frequency Method for Radome Analysis (Meng et al., 2009a)**

### **2.1 General Steps**

The AI-SI method is a high-frequency approximate method and can analyze the electrically large radome in millimeter wave band efficiently. It was introduced to analyze the antenna-

radome system by Paris [Paris, 1970] and many other researchers have done a lot of work on it [Kozakoff, 1997, Meng et al., 2008a]. The general steps of this method are as follows:

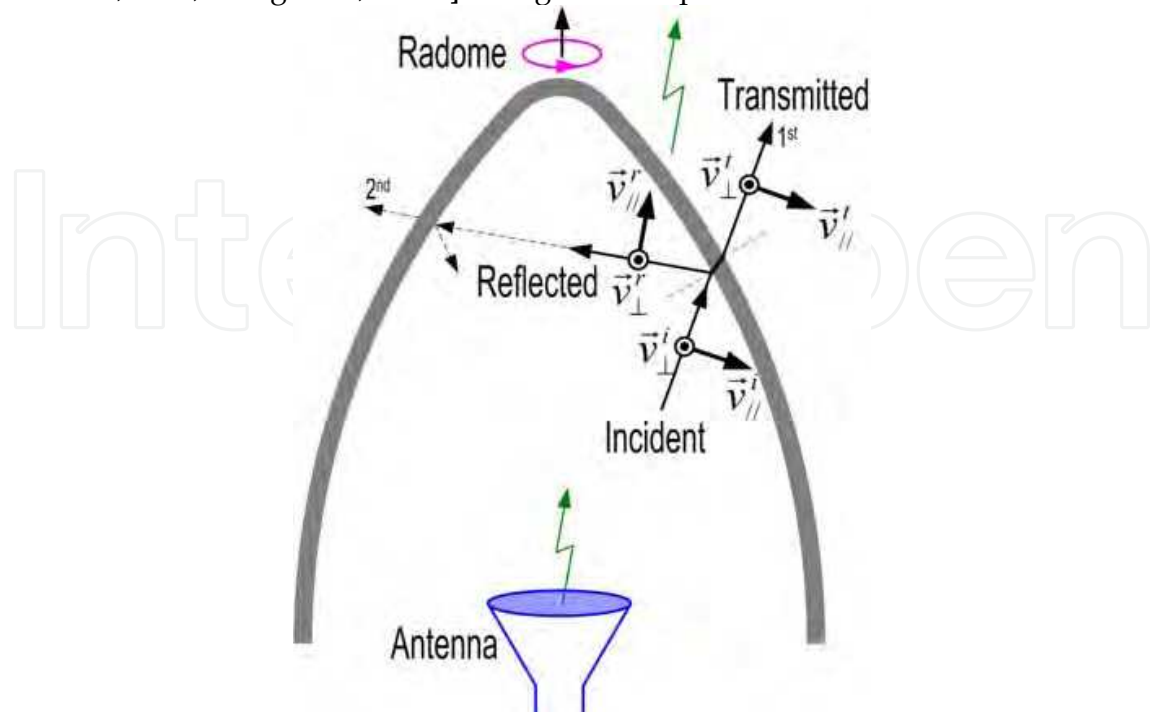


Fig. 1. Model of the AI-SI method for the antenna-radome analysis.

When the electromagnetic fields on the aperture of the antenna are known, the incident wave on the inner surface of the radome can be obtained by integrating over the aperture using the Stratton-Chu formulas. The incident vector at the intersection point on the inner surface of the radome is established by the direction of the Poynting vector [Wu & Rudduck, 1974]

$$\hat{S}_i = \text{Re}(\vec{E}_i \times \vec{H}_i^*) / |\text{Re}(\vec{E}_i \times \vec{H}_i^*)| \quad (1)$$

where  $\vec{E}_i$  and  $\vec{H}_i$  are the incident fields at the intersection point.

The incident vector and the normal vector at the intersection point on the inner surface define the plane of incidence. The incident fields at the intersection point are decomposed into the perpendicular and parallel polarization components to the plane of incidence. After reflection and refraction in the radome wall, the reflected fields  $\vec{E}_r, \vec{H}_r$  and the transmitted fields  $\vec{E}_t, \vec{H}_t$  are recombined as

$$\begin{aligned} \vec{E}_r &= (\vec{E}_i \cdot \vec{v}_\perp^i) R_\perp \vec{v}_\perp^r + (\vec{E}_i \cdot \vec{v}_\parallel^i) R_\parallel \vec{v}_\parallel^r \\ \vec{H}_r &= (\vec{H}_i \cdot \vec{v}_\perp^i) R_\parallel \vec{v}_\perp^r + (\vec{H}_i \cdot \vec{v}_\parallel^i) R_\perp \vec{v}_\parallel^r \end{aligned} \quad (2)$$

$$\begin{aligned} \vec{E}_t &= (\vec{E}_i \cdot \vec{v}_\perp^i) T_\perp \vec{v}_\perp^t + (\vec{E}_i \cdot \vec{v}_\parallel^i) T_\parallel \vec{v}_\parallel^t \\ \vec{H}_t &= (\vec{H}_i \cdot \vec{v}_\perp^i) T_\parallel \vec{v}_\perp^t + (\vec{H}_i \cdot \vec{v}_\parallel^i) T_\perp \vec{v}_\parallel^t \end{aligned} \quad (3)$$

where  $\vec{v}_\perp$  and  $\vec{v}_\parallel$  are the unit vectors illustrated in Fig.1, the superscripts  $i, r$  and  $t$  represent the incident, reflected, and transmitted fields, respectively.  $R_\perp, R_\parallel, T_\perp, T_\parallel$  are the reflection and transmission coefficients for the perpendicular and parallel polarizations, and they will be discussed later.

The reflected wave on the inner surface may bounce between the opposite sides of the radome. At this time, it is regarded as the incident wave for the second time step as an ordinary incident wave. The same process is repeated for the 3rd, 4th...inner reflections. Finally the total fields on the outer surface of the radome are the vector sum of the 1st, 2nd... transmitted fields.

When the fields on the outer surface are known, the far field radiation pattern of the antenna-radome system can be determined by integrating the fields over the outer surface of the radome using the Stratton-Chu formulas again.

## 2.2 Modified Transmission Coefficient

Now, we will concentrate on the reflection coefficients  $R_{\perp}$ ,  $R_{\parallel}$  and the transmission coefficients  $T_{\perp}$ ,  $T_{\parallel}$  in (2) and (3).

When a planar wave is incident from medium  $i$  to medium  $j$ , the Snell's law must be satisfied on the interface. The Fresnel reflection and refraction coefficients for the perpendicular and parallel polarizations are given by [Ishimaru, 1991]

$$\begin{aligned} r_{ij}^{\perp} &= \frac{Z_j \cos \theta_i - Z_i \cos \theta_j}{Z_j \cos \theta_i + Z_i \cos \theta_j} & r_{ij}^{\parallel} &= \frac{Z_i \cos \theta_i - Z_j \cos \theta_j}{Z_i \cos \theta_i + Z_j \cos \theta_j} \\ t_{ij}^{\perp} &= \frac{2Z_j \cos \theta_i}{Z_j \cos \theta_i + Z_i \cos \theta_j} & t_{ij}^{\parallel} &= \frac{2Z_i \cos \theta_i}{Z_i \cos \theta_i + Z_j \cos \theta_j} \end{aligned} \quad (4)$$

where  $Z_i = Z_0 \sqrt{\mu_i / \epsilon_i}$  and  $Z_j = Z_0 \sqrt{\mu_j / \epsilon_j}$  are the characteristic impedances of the two media,  $Z_0$  is the characteristic impedance of free space,  $\epsilon_i, \epsilon_j, \mu_i, \mu_j$  are the relative permittivities and permeabilities of the two media, and  $\theta_i, \theta_j$  are the angles of incidence and refraction, respectively.

For the antenna-radome system in millimeter wave band, the radome is always far away from the antenna, and the curvature radius of the radome is larger than the wavelength, so the incidence of the radiation field upon the radome wall can be simulated as locally planar wave impinging upon locally planar dielectric. In this case, the transmission coefficient of the dielectric plane is always determined by the transmission line analogy [Kozakoff, 1997].

As shown in Fig.2, the N-layered dielectric plane is equivalent to the cascade of the transmission lines with different impedances. For the  $n^{\text{th}}$  equivalent transmission line, the length is  $d_n$ , the equivalent propagation constant is  $k_n \cos \theta_n$ , and the effective impedances of the perpendicular and parallel polarizations are  $Z_n^{\perp} = Z_n \sec \theta_n$  and  $Z_n^{\parallel} = Z_n \cos \theta_n$ , in which  $\theta_n$  is the angle of refraction and  $Z_n = Z_0 \sqrt{\mu_n / \epsilon_n}$  is the characteristic impedance in this layer.

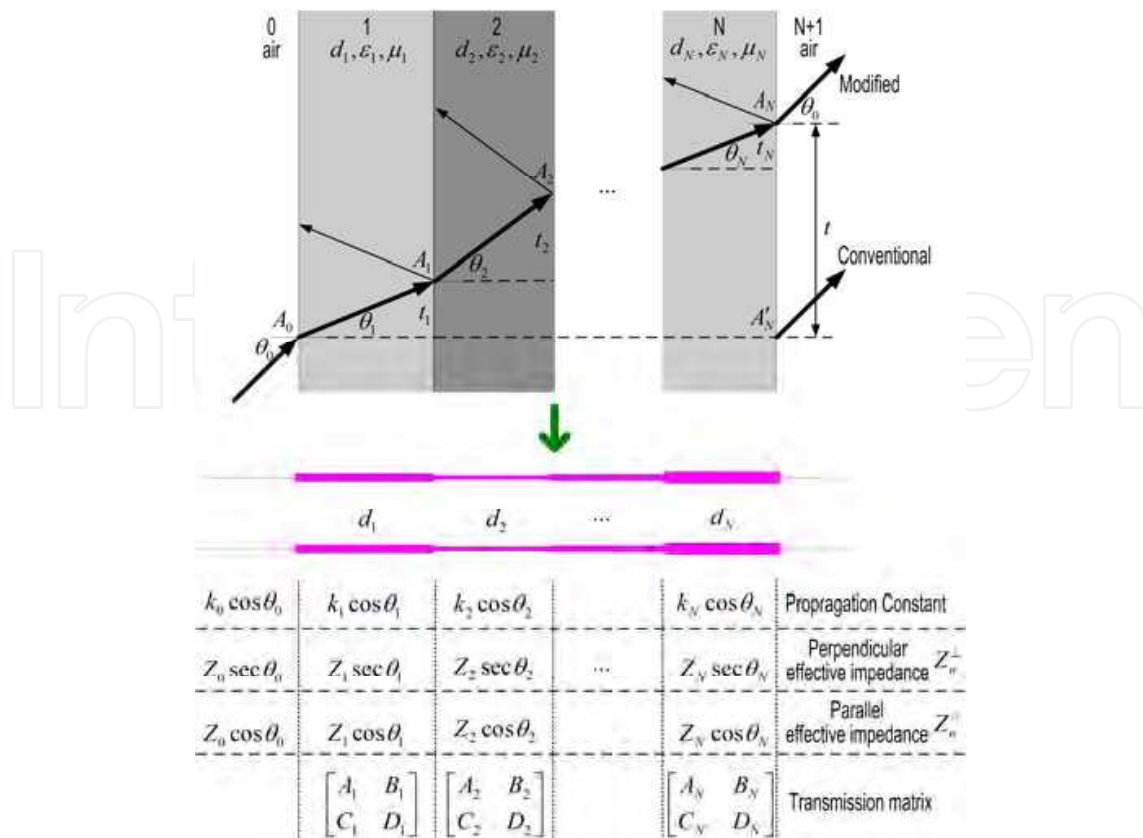


Fig.2. Transmission line analogy of the multi-layered dielectric plane.

For the perpendicular polarization, the transmission matrix of the n<sup>th</sup> layer is

$$\begin{bmatrix} A_n & B_n \\ C_n & D_n \end{bmatrix} = \begin{bmatrix} \cosh(jk_n \cos \theta_n d_n) & Z_n^\perp \sinh(jk_n \cos \theta_n d_n) \\ \sinh(jk_n \cos \theta_n d_n)/Z_n^\perp & \cosh(jk_n \cos \theta_n d_n) \end{bmatrix} \tag{5}$$

Therefore, the transmission matrix of the N-layered dielectric plane is the cascade of the transmission matrix of each layer

$$\begin{bmatrix} A & B \\ C & D \end{bmatrix} = \begin{bmatrix} A_1 & B_1 \\ C_1 & D_1 \end{bmatrix} \begin{bmatrix} A_2 & B_2 \\ C_2 & D_2 \end{bmatrix} \dots \begin{bmatrix} A_N & B_N \\ C_N & D_N \end{bmatrix} \tag{6}$$

Then, the conventional reflection and transmission coefficients of the multi-layered dielectric plane are determined by the network theory as [Ishimaru, 1991]

$$R_\perp = \frac{(A + B/Z_{N+1}^\perp) - Z_0^\perp(C + D/Z_{N+1}^\perp)}{(A + B/Z_{N+1}^\perp) + Z_0^\perp(C + D/Z_{N+1}^\perp)}$$

$$T_\perp = \frac{2}{(A + B/Z_{N+1}^\perp) + Z_0^\perp(C + D/Z_{N+1}^\perp)} \tag{7}$$

For the parallel polarization, the reflection and transmission coefficients can be determined by replacing the perpendicular effective impedance  $Z_n^\perp$  in (5-7) with the parallel effective impedance  $Z_n^\parallel$ , and the results are given by

$$R_{\parallel} = \frac{(A + B/Z_{N+1}^\parallel) - Z_0^\parallel (C + D/Z_{N+1}^\parallel)}{(A + B/Z_{N+1}^\parallel) + Z_0^\parallel (C + D/Z_{N+1}^\parallel)} \quad (8)$$

$$T_{\parallel} = \frac{2}{(A + B/Z_{N+1}^\parallel) + Z_0^\parallel (C + D/Z_{N+1}^\parallel)}$$

As indicated in Fig.2, when a planar wave is propagating in the dielectric plane, the equivalent propagation constants of the equivalent transmission lines are only the longitudinal components of the propagation constants in the dielectrics, and the departure point is at  $A'_N$ . By tracing the ray in the dielectrics, it is clearly that the main route of the wave passing through the dielectric plane is  $A_0 A_1 \dots A_N$ , and the departure point of the wave on the back surface is at  $A_N$ . Therefore, there is a lateral displacement  $t$  between the incident point  $A_0$  and the departure point  $A_N$ .

In the  $n^{\text{th}}$  layer, the transmission distance of the wave in the lateral direction is

$$t_n = d_n \tan \theta_n \quad (9)$$

and the lateral component of the propagation constant is

$$k_n^r = k_n \sin \theta_n \quad (10)$$

From the Snell's law

$$k_0 \sin \theta_0 = k_1 \sin \theta_1 = \dots = k_n \sin \theta_n = \dots = k_N \sin \theta_N \quad (11)$$

we can get the lateral transmission phase shift in the  $n^{\text{th}}$  layer

$$\varphi_n^r = k_n^r t_n = k_n \sin \theta_n \cdot d_n \tan \theta_n = k_0 \sin \theta_0 d_n \tan \theta_n \quad (12)$$

For the N-layered dielectric plane, the total lateral phase shift from  $A_0$  to  $A_N$  is the sum of the phase shift in each layer

$$\begin{aligned} \varphi^r &= \varphi_1^r + \varphi_2^r + \dots + \varphi_N^r \\ &= k_0 \sin \theta_0 d_1 \tan \theta_1 + k_0 \sin \theta_0 d_2 \tan \theta_2 + \dots + k_0 \sin \theta_0 d_N \tan \theta_N \\ &= k_0 \sin \theta_0 (d_1 \tan \theta_1 + d_2 \tan \theta_2 + \dots + d_N \tan \theta_N) \\ &= k_0 \sin \theta_0 (t_1 + t_2 + \dots + t_N) \\ &= k_0 \sin \theta_0 t \end{aligned} \quad (13)$$

in which

$$t = d_1 \tan \theta_1 + d_2 \tan \theta_2 + \dots + t_N \tan \theta_N \quad (14)$$

In order to simulate the wave propagating through the dielectric plane more exactly, the lateral phase shift must be taken into consideration. Thus, we modify the transmission coefficient determined by the transmission line analogy with the following lateral phase factor

$$P^\tau = e^{-j\phi^\tau} = e^{-jk_0 \sin \theta_0 t} \quad (15)$$

Then, we get the modified transmission coefficient for the perpendicular polarization

$$T_\perp^m = T_\perp P^\tau = \frac{2}{\left(A + B/Z_{N+1}^\perp\right) + Z_0^\perp \left(C + D/Z_{N+1}^\perp\right)} e^{-jk_0 \sin \theta_0 t} \quad (16)$$

Whereas, for the parallel polarization, there is

$$T_\parallel^m = T_\parallel P^\tau = \frac{2}{\left(A + B/Z_{N+1}^\parallel\right) + Z_0^\parallel \left(C + D/Z_{N+1}^\parallel\right)} e^{-jk_0 \sin \theta_0 t} \quad (17)$$

### 2.3 Numerical and Experimental Results

In order to verify the modification of the transmission coefficient, an antenna-radome system at W-band is investigated experimentally. The measured radiation patterns are compared with the calculated results.

The conical radome is shown in Fig.3. The radome has a height of 200mm and a base diameter of 156mm. In the front part of the radome, there is a dome with the curvature radius of 8mm. This radome with the thickness of 5mm is made of Teflon. The permittivity of the dielectric is 2.1. A conical horn with the aperture diameter of 20mm is enclosed by the radome. The horn can rotate around the gimbal center, which is located at the base center of the radome. The antenna-radome system is operating at 94GHz.

When the antenna points to the axial direction of the radome, Fig.3 shows the radiation patterns of the antenna-radome system calculated with the modified transmission coefficient and the conventional one. The measured radiation patterns are also given in these figures. In Fig.3 (a), the calculated E plane radiation pattern with the conventional transmission coefficient is wider than the measured pattern, and the result of the modified one agrees with the measured pattern much better. In the H plane as given in Fig.3 (b), the modified transmission coefficient predicts the sidelobe level of the pattern precisely; however, the calculated radiation pattern with the conventional transmission coefficient has an error of 5dB comparing with the measured data.

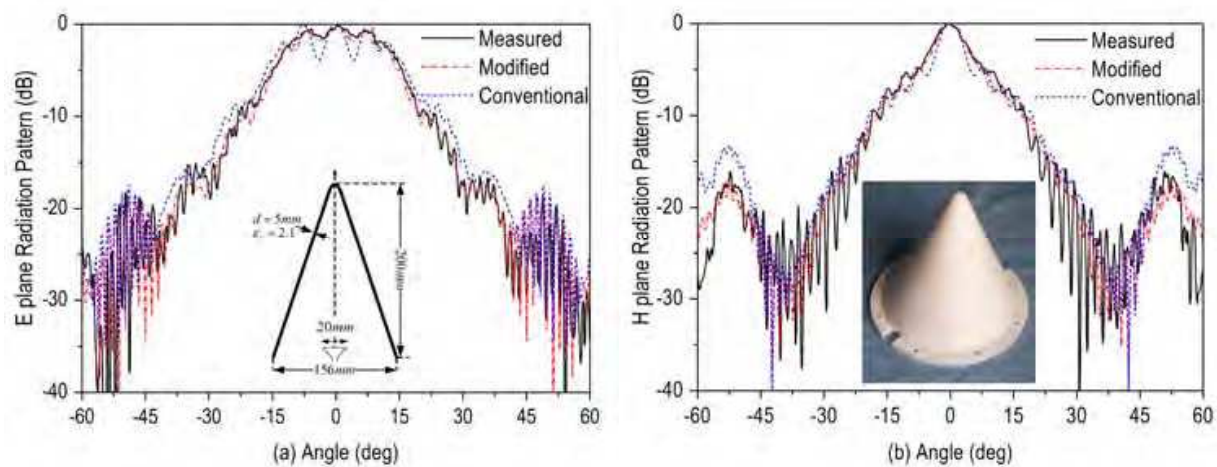


Fig.3. Measured and calculated radiation patterns of the conical horn enclosed by the conical radome: (a) E plane, (b) H plane.

Then, the antenna tilts  $10^\circ$  in the E plane and H plane respectively. The calculated radiation patterns with the two transmission coefficients and the measured results are illustrated in Fig.4. Comparing these radiation patterns, the patterns calculated with the modified transmission coefficient have good agreements with the measured results; however, there is an error of 7dB in the left sidelobe between the measured H plane pattern and the one calculated with the conventional transmission coefficient.

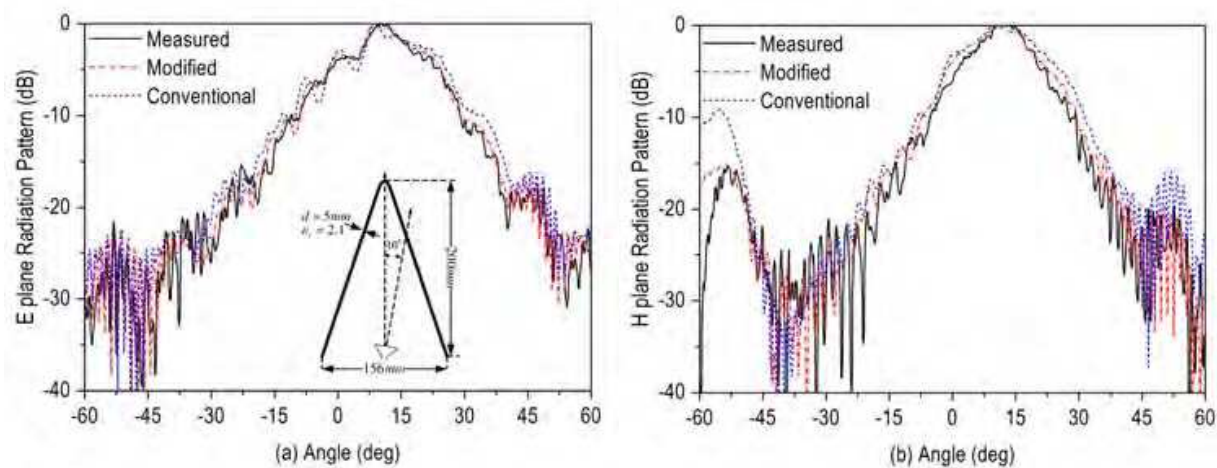


Fig.4. Measured and calculated radiation patterns of the conical horn enclosed by the conical radome when the horn tilts  $10^\circ$  in the E plane and H plane respectively: (a) E plane, (b) H plane.

### 3. Hybrid Method for Radome Analysis (Meng & Dou, 2009b)

#### 3.1 General Steps

As illustrated in Fig.5, the radome is divided into two parts: a) LF region with the length of  $L_{LF}$  from the vertex of the radome, in which there are complex structures. b) HF region, the

remainder portion of the radome with the length of  $L_{HF}$ , where the surface is smooth and the curvature radius is larger than the wavelength.

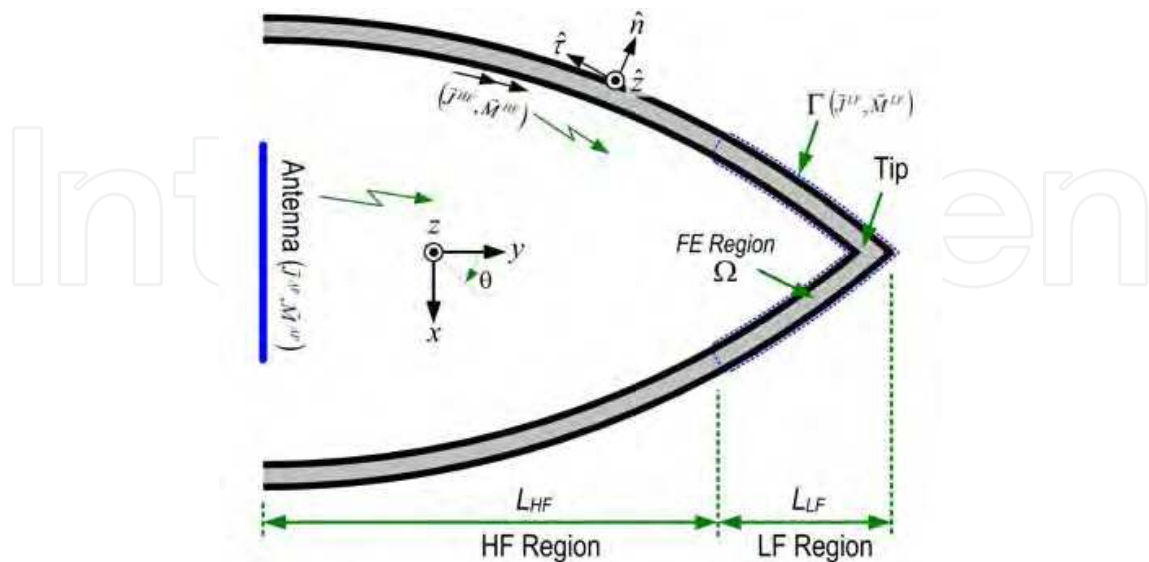


Fig. 5. Configurations of the electrically large A-sandwich tangogive radome

In the HF region, the radome surface is smooth and the curvature radius is much larger than the wavelength, so the assumption of locally planar dielectric can be adopted. The AI-SI method has been found very efficient and can get acceptable result for this structure.

Firstly, the incident fields  $(\vec{E}_i, \vec{H}_i)$  on the inner surface of the radome are assumed only the radiation fields from the antenna as the traditional antenna-radome analysis [Abdel et al., 2001].

$$\begin{aligned} \vec{E}_i &= E_J(\vec{J}^{Ap}) + E_M(\vec{M}^{Ap}) \\ \vec{H}_i &= H_J(\vec{J}^{Ap}) + H_M(\vec{M}^{Ap}) \end{aligned} \tag{18}$$

where  $(\vec{J}^{Ap}, \vec{M}^{Ap})$  are the electric and magnetic currents on the aperture of antenna, and the operators  $E_J(\vec{J})$  and  $E_M(\vec{M})$  are defined as:

$$\begin{aligned} E_J(\vec{J}) &= -jk_0 Z_0 \int_S \vec{J} G(r, r') dr' \\ E_M(\vec{M}) &= \int_S \vec{M} \frac{\partial G(r, r')}{\partial n'} dr' \end{aligned} \tag{19}$$

in which  $S$  is the aperture of the antenna and  $G(r, r')$  is the 2D free space green's function. The operators  $H_M(\vec{M})$  and  $H_J(\vec{J})$  in (18) are duality of (19).

Then, the reflected fields  $(\vec{E}_r, \vec{H}_r)$  on the inner surface and the transmitted fields  $(\vec{E}_t, \vec{H}_t)$  on the outer surface of the radome can be determined by transmission line analogy as in [IP & Yahaya, 1998]. The equivalent currents on the inner surface of the HF region of the radome are determined by equivalence theorem as follows

$$\begin{aligned}\vec{J}^{HF} &= \hat{n} \times (\vec{H}_i + \vec{H}_r) \\ \vec{M}^{HF} &= -\hat{n} \times (\vec{E}_i + \vec{E}_r)\end{aligned}\quad (20)$$

and the currents on the outer surface are

$$\begin{aligned}\vec{J}^{HF} &= \hat{n} \times \vec{H}_t \\ \vec{M}^{HF} &= -\hat{n} \times \vec{E}_t\end{aligned}\quad (21)$$

where  $\hat{n}$  is the unit normal vector on the surface of the radome.

For 2D TM case, the electrical field  $E_z$  in the LF region satisfies the following Helmholtz equation

$$\begin{cases} \frac{\partial}{\partial x} \left( \frac{1}{\mu_r} \frac{\partial E_z}{\partial x} \right) + \frac{\partial}{\partial y} \left( \frac{1}{\mu_r} \frac{\partial E_z}{\partial y} \right) + k_0^2 \varepsilon_r E_z = 0 & \text{in } \Omega \\ \frac{1}{\mu_r} \frac{\partial E_z}{\partial n} = jk_0 Z_0 J_z & \text{on } \Gamma \end{cases}\quad (22)$$

where  $\Omega$  is the interior area of the FE region and  $\Gamma$  is its boundary.  $J_z$  is the unknown electric current on  $\Gamma$ .  $\varepsilon_r, \mu_r$  are the relative permittivity and permeability in  $\Omega$ . For the non-uniform region,  $\varepsilon_r, \mu_r$  are the functions of the position.

The field  $E_z$  can be solved by minimizing the following functional [Jin, 1993]

$$\begin{aligned}F(E_z) &= \frac{1}{2} \iint_{\Omega} \left[ \frac{1}{\mu_r} \left( \frac{\partial E_z}{\partial x} \right)^2 + \frac{1}{\mu_r} \left( \frac{\partial E_z}{\partial y} \right)^2 - k_0^2 \varepsilon_r E_z^2 \right] d\Omega \\ &+ jk_0 Z_0 \int_{\Gamma} E_z J_z d\Gamma\end{aligned}\quad (23)$$

As described in [Jin, 1993], the field  $E_z$  in  $\Omega$  is expanded in terms of finite element function defined in triangle and the electric current  $J_z$  is expanded using the triangular basis function. Applying the finite element analysis to (23), the linear equation of FEM is obtained as follows:

$$\begin{bmatrix} K_{II} & K_{IS} & 0 \\ K_{SI} & K_{SS} & B \end{bmatrix} \begin{bmatrix} E_I^{LF} \\ E^{LF} \\ J^{LF} \end{bmatrix} = \begin{bmatrix} 0 \\ 0 \end{bmatrix}\quad (24)$$

where  $K, B$  are the coefficient matrices,  $E_I^{LF}$  is the field in  $\Omega$  and  $E^{LF}, J^{LF}$  are the field and current on  $\Gamma$ , respectively.

The LF region can also be analyzed as a scattering problem. The scatter is the LF region of radome and the excitation is the radiation fields from the antenna and the PO currents on

HF region together. The electric field integral equation in the exterior of LF region is established as

$$\vec{E}^{LF} - E_J(\vec{J}^{LF}) - E_M(\vec{M}^{LF}) = \vec{E}_i \quad (25)$$

where  $\vec{J}^{LF}, \vec{M}^{LF}$  are the unknown currents on the boundary  $\Gamma$  and the incident field  $\vec{E}_i$  is sum of the following parts:

$$\vec{E}_i = E_J(\vec{J}^{Ap}) + E_M(\vec{M}^{Ap}) + E_J(\vec{J}^{HF}) + E_M(\vec{M}^{HF}) \quad (26)$$

in which  $E_J(\vec{J}^{Ap}), E_M(\vec{M}^{Ap})$  are the radiation fields from the aperture antenna and  $E_J(\vec{J}^{HF}), E_M(\vec{M}^{HF})$  are the fields radiated by the PO currents of the HF region.

Then, MoM is applied to equation (25). On the boundary  $\Gamma$  we have the relationship of

$$E^{LF} \hat{\tau} = E^{LF} \hat{z} \times \hat{n} = \vec{E}^{LF} \times \hat{n} = \vec{M}^{LF} = M^{LF} \hat{\tau} \quad (27)$$

So the currents  $J^{LF}, M^{LF}$  are expanded in terms of triangular basis functions and the Galekin's testing is employed. We obtain the following matrix equation:

$$\begin{bmatrix} P & Q \end{bmatrix} \begin{bmatrix} M^{LF} \\ J^{LF} \end{bmatrix} = [b] \quad (28)$$

where P, Q are the coefficient matrices of MoM and b is the excitation column.

As we have the relationship of (27) on the boundary  $\Gamma$ , we find that (24) and (28) have the same unknowns  $M^{LF}, J^{LF}$ . Combining the two equations together, we obtain the hybrid equation of PO-BI-FEM [Jin, 1993]

$$\begin{bmatrix} K_{II} & K_{IS} & 0 \\ K_{SI} & K_{SS} & B \\ 0 & P & Q \end{bmatrix} \begin{bmatrix} E_i^{LF} \\ M^{LF} \\ J^{LF} \end{bmatrix} = \begin{bmatrix} 0 \\ 0 \\ b \end{bmatrix} \quad (29)$$

Solving this hybrid equation, the currents  $J^{LF}, M^{LF}$  on the boundary  $\Gamma$  of the LF region are obtained. The currents  $J^{HF}, M^{HF}$  in HF region are already determined by PO modeling in (20) (21), then the far field radiation pattern of the antenna-radome system can be determined by integrating the currents over the outer surface of the radome.

In our former PO modeling, the incident fields (18) on the inner surface of the radome are assumed only the radiated fields from the antenna and the mutual interactions among the different parts of the radome are ignored. Actually, the equivalent currents  $\vec{J}^{LF}, \vec{M}^{LF}, \vec{J}^{HF}$ , and  $\vec{M}^{HF}$  on the surface of the radome will radiate for the second time (secondary radiation).

In order to take this high-order interaction into radome analysis, we modify the incident fields (18) on the inner surface of the radome by

$$\begin{aligned}\vec{E}_i &= E_J(\vec{J}^{Ap}) + E_M(\vec{M}^{Ap}) \\ &+ E_J(\vec{J}^{HF}) + E_M(\vec{M}^{HF}) + E_J(\vec{J}^{LF}) + E_M(\vec{M}^{LF}) \\ \vec{H}_i &= H_J(\vec{J}^{Ap}) + H_M(\vec{M}^{Ap}) \\ &+ H_J(\vec{J}^{HF}) + H_M(\vec{M}^{HF}) + H_J(\vec{J}^{LF}) + H_M(\vec{M}^{LF})\end{aligned}\quad (30)$$

These new incident fields are the sum of the fields from the antenna aperture and the surface currents on the radome. The other steps are the same as before and we repeat the antenna-radome analysis again. After the second iteration, the currents on the surface of the radome are updated and the radiation pattern is calculated again.

It can be predicted that the results of the second iteration are more accurate because of approximately considering the mutual interactions of the radome. In a similar way, we can determine the secondary radiation fields using the updated currents, and then we start the third iteration. The same process can be done for the fourth, fifth... iteration. As more iteration is done, the results will be more accurate; however, it will cost more time. Compromising between the accuracy and efficiency, when the results of two adjacent iterations have no significant difference, the iterative step can be stopped.

### 3.2 Numerical Results

Firstly, a moderate size A-sandwich tangent ogive radome is analyzed using the present IPO-BI-FEM and the results are compared with that of the full wave method to verify the validity of the method. The three-layered radome is  $17.3\lambda_0$  in length,  $20\lambda_0$  in based diameter with the thicknesses of  $0.08\lambda_0, 0.12\lambda_0, 0.08\lambda_0$  and dielectric relative permittivity of 4.0, 1.8, and 4.0, respectively. An antenna with the aperture diameter of  $5.5\lambda_0$  locates at the base center of the radome. The aperture currents are cosine distribution. The section with the length of  $L_{LF} = 2.5\lambda_0$  from the tip is chosen as the LF region and the other smooth portion of the radome is HF region.

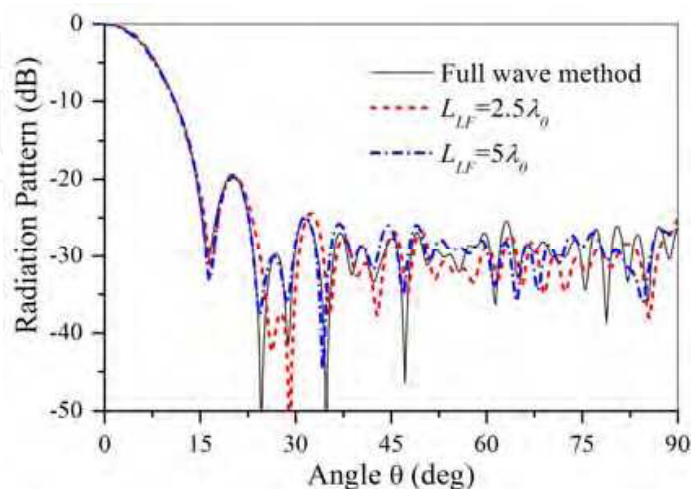


Fig.6. Radiation patterns of the A-sandwich tangent ogive radome determined by full wave method and IPO-BI-FEM with  $L_{LF} = 2.5\lambda_0$  and  $L_{LF} = 5.0\lambda_0$

The normalized radiation pattern of the antenna-radome system determined by IPO-BI-FEM after three iterations is given in Fig.6. The result determined by the full wave method is also shown as a comparison. It is clear that, the main lobe and first side lobe of the pattern determined by IPO-BI-FEM agree well with the full wave result, but some differences appear in the far side lobes. As in Fig.6, when the LF region extends to  $L_{LF} = 5.0\lambda_0$ , the second and third side lobes are also well predicted and the other side lobes are more close to the reference. It can be predicted that as the LF region becomes longer, the radiation pattern will agree better with the full wave result, but it will cost more time. When  $L_{LF}$  is set as the total length of the radome, the hybrid method becomes pure BI-FEM, which is a full wave method, and our reference result is obtained, but the efficiency is lowest. Considering the accuracy and efficiency of the hybrid method, setting  $L_{LF}$  about  $5\lambda_0$  from the tip is a compromise.

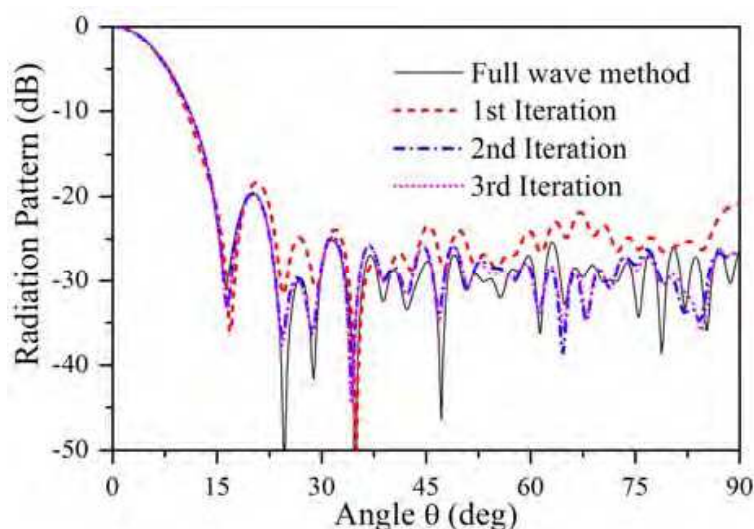


Fig. 7. Radiation patterns of the A-sandwich radome determined by the full wave method and IPO-BI-FEM in different iteration

Fig.7 shows the normalized radiation patterns of the tangent ogive radome in the three iterations when simulated using IPO-BI-FEM with  $L_{LF} = 5.0\lambda_0$ . It is seen that, the pattern of the first iteration has considerable differences with that determined by full wave method; however, the patterns of the second and third iteration are about the same and both agree very well with the reference result. As the mutual interactions of the radome are accounted in the last two iterations, this iterative use of the hybrid method indeed improve the accuracy of the result, but it need additional time for the iteration. In practical simulation, three iterations are enough to obtain the convergent results.

At the same time, IPO-BI-FEM only spends 31 minutes to simulate this moderate size radome; however, the full wave method takes about 4 hours and 10 minutes. A reduction in CPU time by a factor of 8 is reached. The improvement of efficiency of the present method is obvious. For electrically large radome, the efficiency of the present method will be much higher.

Then, an electrically large A-sandwich radome as in Fig.5 is analyzed as the first application. This radome is also tangent ogive shape with the electrically large size of  $100\lambda_0$  in length and  $80\lambda_0$  in base diameter. The thicknesses of the three layers are  $0.035\lambda_0$ ,  $0.33\lambda_0$  and  $0.035\lambda_0$ . The

three layers are low lossy dielectrics with the permittivity of 4.0, 1.8, 4.0 and loss tangent of 0.002, 0.001, and 0.002, respectively. An antenna with the diameter of  $20\lambda_0$  is located at the base center of the radome. The aperture distribution is cosine function. Two different LF region lengths ( $L_{LF} = 5.0\lambda_0, 10.0\lambda_0$ ) are chosen. This radome is simulated by IPO-BI-FEM with three iterations. The radiation patterns of this antenna-radome system are compared with the pattern of the antenna without radome in Fig.8. As we can see, when the radome is covered, there is an attenuation of 1.1dB in the maximal gain, a shoulder appears in the main lobe, and all the far side lobes are raised significantly. Comparing the radiation patterns determined with  $L_{LF} = 5.0\lambda_0$  and  $L_{LF} = 10.0\lambda_0$ , the main lobe and the first two side lobes are very close to each other, which verifies the convergence of IPO-BI-FEM.

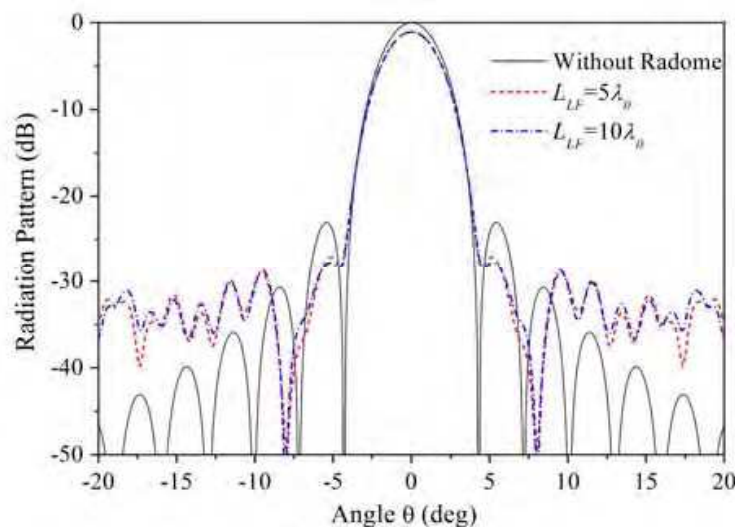


Fig. 8. Radiation patterns of the antenna without radome and with the electrically large A-sandwich tangent ogive radome when  $L_{LF} = 5.0\lambda_0$  and  $L_{LF} = 10.0\lambda_0$

For the antenna-radome system on high-speed aircraft, the radome always suffers from the rain erosion, especially in the tip region. In the purpose of overcoming this problem, a metallic cap is covered in the front of the radome to protect the radome (Fig.9). Unfortunately, very little open literature is available for accurately analyzing this complex radome [Kozakoff, 1997]. However, it can be analyzed easily by the presented hybrid method.

As in Fig.9, the radome with the length of  $86\lambda_0$ , base diameter of  $30\lambda_0$ , and thickness of  $0.32\lambda_0$  has a Von-Karman outer profile to satisfy the aerodynamic requirement. The metallic cap with the thickness of  $1.0\text{mm}$  is embedded in the front of radome to resist the rain erosion. A phase array antenna with 26 elements and element distance of  $6.5\text{mm}$  can rotate around the gimbal, which is  $200\text{mm}$  from the base center of the radome. The operating frequency is at Ka band.

In our model, the radomes with three different sizes of metallic cap are investigated. They are  $D_c = 0\text{mm}$  (means without metallic cap),  $12\text{mm}$ , and  $18\text{mm}$  respectively. The LF region is extended  $5\lambda_0$  from the cap. The radiation patterns of the antenna-radome system with different metallic caps are compared in Fig. 10. The radiation pattern of the array antenna without radome is also given as a reference. It is clear that, the radome without metallic cap

only induces an attenuation of  $0.4\text{dB}$  in the main beam and the sidelobe level rises from  $-27.3\text{dB}$  to  $-19.4\text{dB}$ . However, when the metallic cap with  $D_c=12\text{mm}$  covered, the attenuation increases to  $1.1\text{dB}$  and all the sidelobe are raised significantly. As the metallic cap increasing to  $D_c=18\text{mm}$ , an additional attenuation of  $0.6\text{dB}$  appears and the side lobes are much higher. This IPO-BI-FEM can analyze the effects of the metallic cap on the antenna-radome system accurately and conveniently.

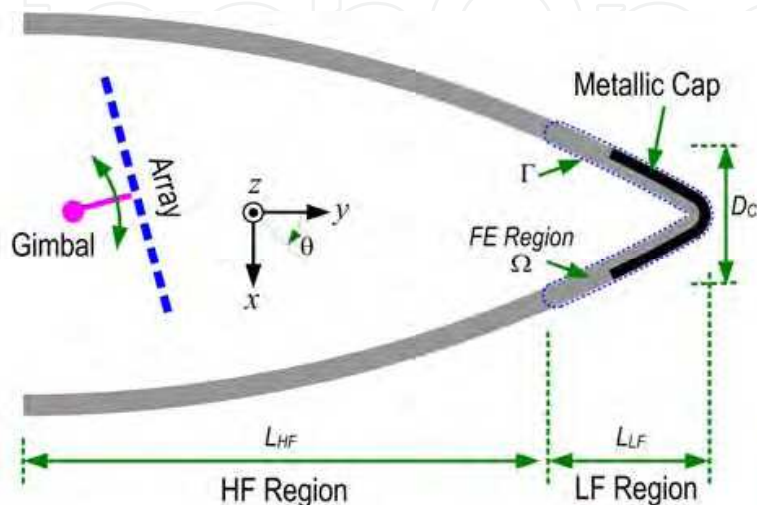


Fig. 9. Configurations of the electrically large Von-Karman radome with metallic cap

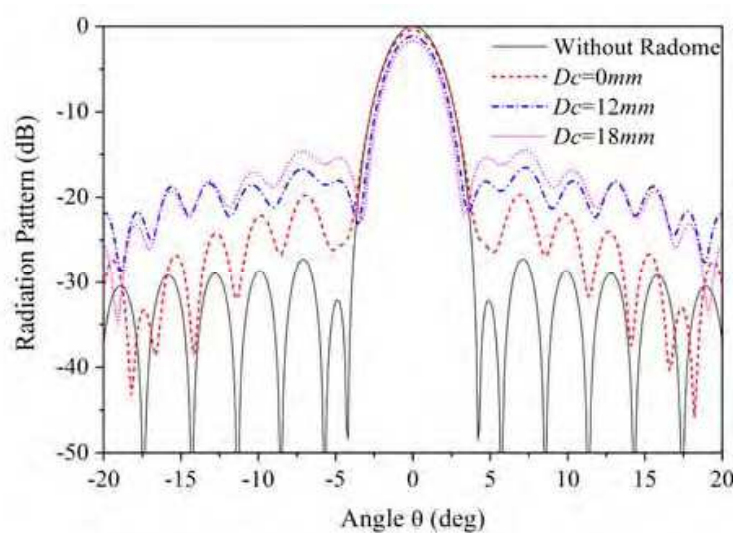


Fig. 10. Radiation patterns of the antenna-radome system with different metallic caps

Then the array antenna tilts with  $10^\circ$  to the left of the  $y$  axis. The radiation patterns of the antenna-radome system are given in Fig. 11. As we can see, when the antenna tilted, the metallic cap is removed from the main beam, the blockages of the cap and the high-order interactions between the metallic cap and radome are much smaller. Compared with the patterns in Fig.10, the influences of these radomes on the radiation patterns of the antenna are much smaller.

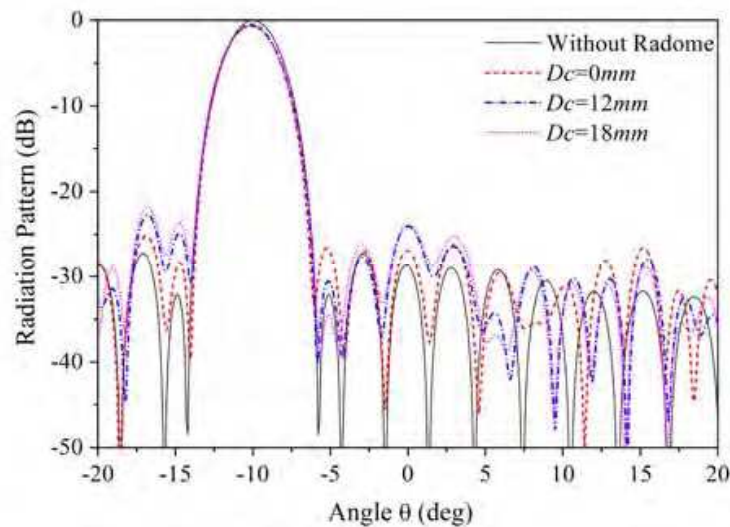


Fig. 11. Radiation patterns of the antenna-radome system when the antenna tilted with  $10^\circ$

## 4. Antenna-radome Optimization (Meng & Dou, 2008b)

### 4.1 General Steps

For the antenna-radome system in millimeter wave band, the electrical sizes of the radome are always very large. The high frequency method, such as RT method [Kozakoff, 1997] is very efficient and can get acceptable results, especially for radome with smooth surface. The RT method assumes that the fields radiate from the aperture of the antenna like a bunch of rays and transmit through the radome as the wall is locally plane at each intercept point. The fields outside the radome are obtained by accounting for the effects of the radome wall on the amplitude and phase of the propagation rays. The radiation performances of the antenna-radome system are determined by integrating the fields over the outer surface of the radome using Stratton-Chu formula.

As the radome wall has different transmission effects on different rays, the radiation patterns of the antenna-radome system are distorted. For the radome covered monopulse antenna, the gain loss of the sum radiation pattern is the power transmittance, and the angular difference between the null direction of the difference radiation pattern and the look angle of the antenna is the BSE induced by the radome. In order to improve the performances of the antenna-radome system, we can change the thicknesses of the radome wall at different parts to compensate the amplitude and phase distortion of the rays.

In general optimization of the radome, the thickness of the radome varies in the entire region [Hsu et al., 1993; Hsu et al., 1994; Nair & Jha, 2007]. However, the grind of this variable thickness radome is very laborious and the accuracy is difficult to control, especially for the electrically large radome in millimeter wave band. For the purpose of overcoming this problem, the region with variable thickness must be as small as possible. Thus, we propose the structure of local uniform thickness radome in the present work. The radome wall is described as below.

The A-sandwich wall consists of two high-density dielectric skins separated by a low-density core having a lower relative permittivity than the skins. The thickness profile  $d(z)$  of the local uniform thickness A-sandwich radome is expressed as the following piecewise function:

$$d(z) = 2d_s + \begin{cases} d_1 & 0 \leq z < z_1 - \lambda \\ f_1(z) & z_1 - \lambda \leq z < z_1 + \lambda \\ d_2 & z_1 + \lambda \leq z < z_2 - \lambda \\ f_2(z) & z_2 - \lambda \leq z < z_2 + \lambda \\ d_3 & z_2 + \lambda \leq z \leq L \end{cases} \quad (31)$$

where  $d_s$  is the thickness of the skin layers,  $d_1$ ,  $d_2$ , and  $d_3$  are the thicknesses of the core layer in the three local uniform regions,  $z_1$ ,  $z_2$  are the locations of the transitional regions as in Fig.12 (a).  $\lambda$  is the wavelength in free space and  $L$  is the total length of the radome. The thickness profile of the radome wall is guaranteed to be smooth by the function  $f_1(z)$ ,  $f_2(z)$  in the transitional regions:

$$\begin{aligned} f_1(z) &= d_1 + \frac{d_2 - d_1}{4\lambda^2} (z - z_1 + \lambda)^2 - \frac{d_2 - d_1}{4\lambda^3} (z - z_1 + \lambda)^2 (z - z_1 - \lambda) \\ f_2(z) &= d_2 + \frac{d_3 - d_2}{4\lambda^2} (z - z_2 + \lambda)^2 - \frac{d_3 - d_2}{4\lambda^3} (z - z_2 + \lambda)^2 (z - z_2 - \lambda) \end{aligned} \quad (32)$$

Compared with the transitional length ( $2\lambda$ ), the thickness changes (from  $d_1$  to  $d_2$  or from  $d_2$  to  $d_3$ ) in the transitional region are very small and the curvature radius of the radome wall is very large, so the RT method is still applicable. The 3D radome is a body of revolution (BOR) by revolving the thickness profile of the radome around the  $z$  axis.

In the optimization process, we employ GA to find the best thicknesses at different parts of the radome. GA is a global optimization method and is more and more popular in electromagnetic engineering [Weile & Michielssen, 1997]. The variables  $d_s$ ,  $d_1$ ,  $d_2$ ,  $d_3$ ,  $z_1$ ,  $z_2$  of the local uniform thickness radome are chosen as the optimal parameters and the objects are to minimize the maximum BSE and maximize the minimum power transmittance when the antenna scans in the desired angle of azimuth (AZ) and elevation (EL) planes. The objective function  $ObjF$  of the GA model is defined as:

$$ObjF = \min_{d(z)} \left\{ \max_{\theta} [BSE(\theta, d(z))] \right\} + \max_{d(z)} \left\{ \min_{\theta} [PTrans(\theta, d(z))] \right\} \quad (33)$$

Where  $\theta$  is the scanning angle in the two planes.  $\min\{f\}$ ,  $\max\{f\}$  are the minimum and maximum of the function  $f$ .  $BSE(f)$ ,  $PTrans(f)$  are the BSE and power transmittance of the desired radome, respectively.

## 4.2 Numerical Results

The configuration of our antenna-radome system is illustrated in Fig.12 (a). The outer profile of the radome is a Von-Karman curve to satisfy the aerodynamic requirement and the inner surface varies with the thickness profile. The radome with the length of  $86\lambda_0$  and the base diameter of  $30\lambda_0$  covers a waveguide slot antenna with a circular aperture. The aperture is divided into four parts to form the sum and difference patterns in the AZ and EL plane, respectively. The antenna can rotate from  $-30^\circ$  to  $+30^\circ$  in the two main planes around the gimbal, which is 200 mm away from the base center of the radome, and the radius of rotation is 50 mm. The two skin layers of the A-sandwich radome have the dielectric with relative permittivity of  $\epsilon_r = 6.0$  and loss tangent of  $\tan \delta = 0.002$ . The core layer is made of foam with  $\epsilon_r = 1.2$  and  $\tan \delta = 0.001$ . The antenna-radome system works at Ka band.

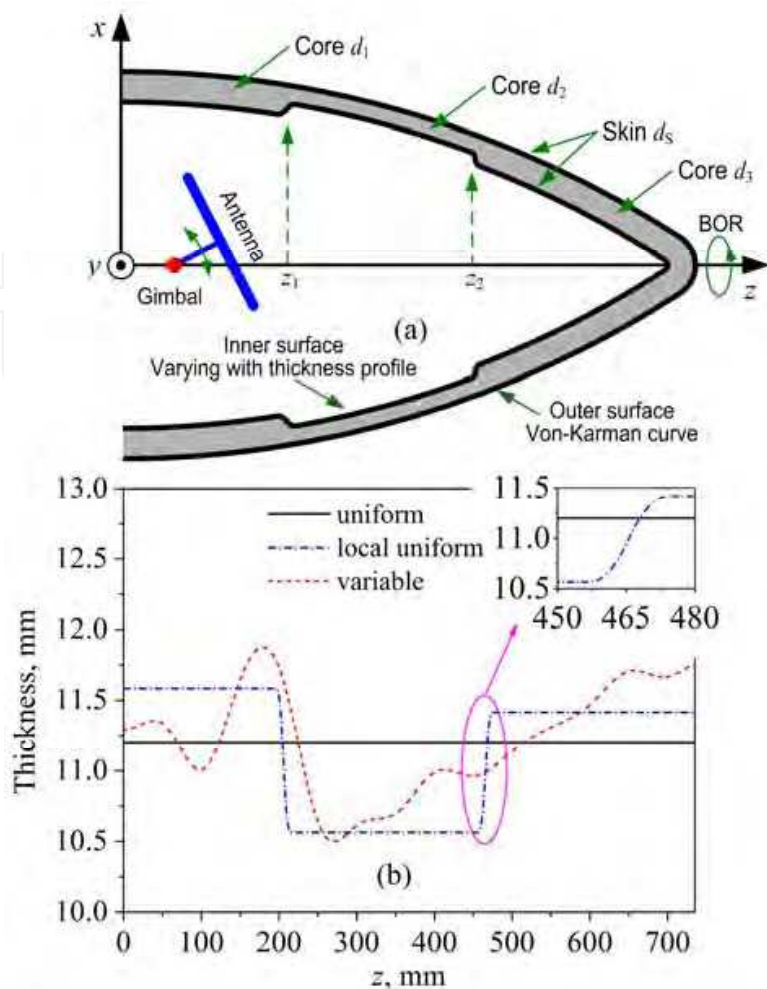


Fig. 12. (a) Configuration of the antenna-radome system, (b) thickness profiles of the uniform, local uniform thickness, and variable thickness radome

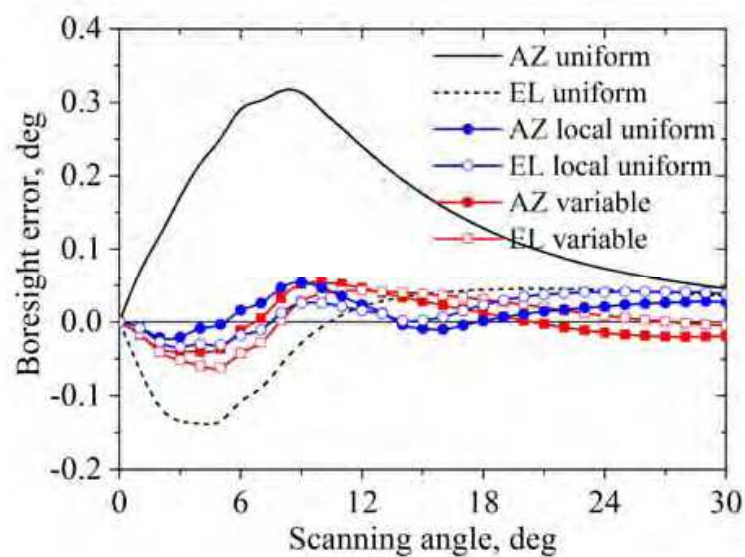


Fig. 13. Boresight errors of the uniform, local uniform thickness, and variable thickness radome in AZ and EL plane

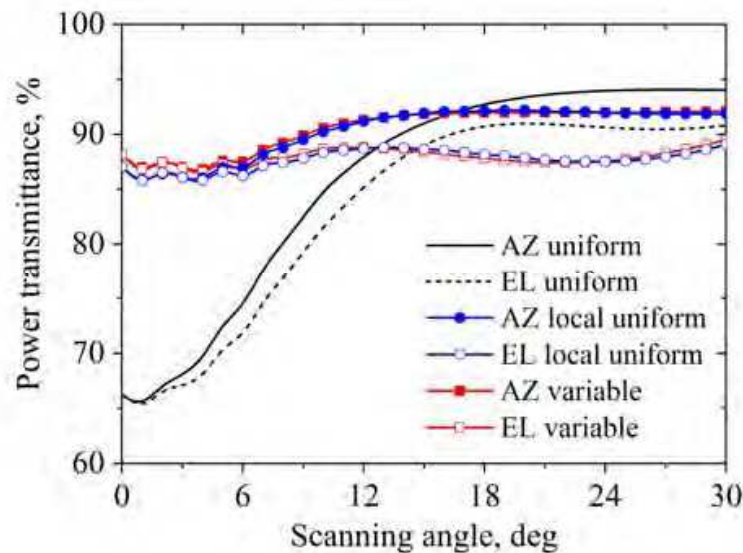


Fig. 14. Power transmittances of the uniform, local uniform thickness, and variable thickness radome in AZ and EL plane

As an example, the proposed structure of local uniform thickness is adopted for the radome optimization. The thicknesses  $d_s$  of two skin layers are limited between 1.7 mm and 2.0 mm, the thicknesses of the core layer in the three local regions can vary from 6.5 mm to 8.5 mm, and the positions of the two transitional regions are constrained as  $0 < z_1 < z_2 < 86\lambda_0$ . After optimization by the multi-objective GA, the optimal thickness profile of the local uniform thickness radome is shown in Fig.12 (b), and the BSE and power transmittance against the scanning angle are given in Fig.13-14. As a reference, the BSE and power transmittance of a uniform thickness radome with the skin thickness of  $d_s=1.85$  mm and uniform core thickness of  $d_c=7.5$  mm are also shown in Fig.13-14. Compared with the results of uniform thickness radome, the maximal BSE of the optimal antenna-radome system is reduced from  $0.3^\circ$  to  $0.05^\circ$  and the minimal power transmittance is increased from 66% to 86%. In the entire scanning range, the changes of the BSE and power transmittance are more slowly, which is more favorable for the radar tracing system. The above results verify the validities of the local uniform thickness radome and the multi-objective optimization model.

The variable thickness optimization described in [Hsu et al., 1994] is also implemented as a comparison. The thicknesses of the skin and core layers are restricted the same as the local uniform optimization. The thickness profile of the optimal radome is shown in Fig.12 (b) and the BSE and power transmittance are also given in Fig.13-14. It is clear that the present local uniform thickness radome obtains the similar BSE and power transmittance as the variable thickness optimization; however, the proposed radome keeps being uniform in most parts of the radome and the thickness only varies in two very small regions, which is easier to be fabricated than the variable thickness radome.

## 5. Conclusion

As the development of millimeter wave technology, the millimeter wave antenna-radome systems have been used more and more popular. In this chapter, we mainly concentrate on the methods for radome analysis and design. The general AI-SI method is modified to

improve the accuracy of millimeter wave radome analysis. The hybrid IPO-BI-FEM method is proposed to deal with the radome with small complex structures. Also, the GA combined with the RT method is adopted to optimize the BSE and power transmittance of the millimeter wave radome. All these methods have been verified validity by the numerical and experimental results. Some analysis and design examples are given.

## 6. Acknowledgment

This work is supported by the National Natural Science Foundation of China under grant 60571028.

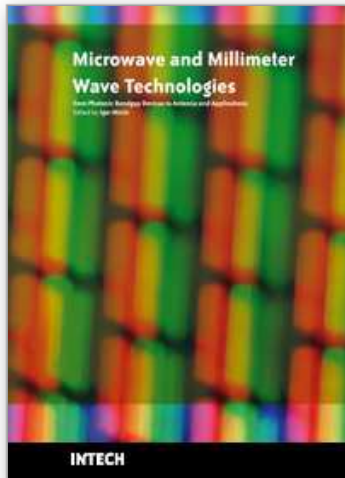
## 7. References

- Abdel Moneum M. A., Shen Z. X., Volakis J. L. and Graham O. (2001), Hybrid PO-MoM Analysis of Large Axi-Symmetric Radomes, *IEEE Trans Antennas Propagat* 49, 1657-1666.
- Arvas E., Rahhalarabi A., Pekel U. and Gundogan E. (1990), Electromagnetic transmission through a small radome of arbitrary shape, *Microwaves, Antennas and Propagation, IEE Proceedings H*, 137(6), 401-405.
- Einzig P. and Felsen L. (1983), Ray annalysis of two-dimensional radomes, *IEEE Transactions on Antenna and Propagation*, 31(6), 870-884.
- Fu wen-bin, Chen Zhong-kuan, and Chang Yi-tao, (2005)“Multi-objective optimization of electric performance of sandwich antenna radome wall using genetic algorithm”, *Chinese Journal of Radio Science*, Vol.20, No.3, pp.289-294,.
- Gao X. J. and Felsen L. B. (1985), Complex ray analysis of beam transmission through two dimensional radomes, *IEEE Transactions on Antenna and Propagation*, 33(9), 963-975.
- Gomez-Revuelto I., Garcia-Castillo L. E., Salazar-Palma M., and Sarkar T. K. (2005), Fully coupled hybrid-method FEM/high-frequency technique for the analysis of 3D scattering and radiation problems, *Microwave Opt Tech Lett* 47, 104-107.
- Gordon R. K. and Mittra R. (1993), Finite element analysis of axisymmetric radomes, *IEEE Trans Antennas Propagat* 41, 975-981.
- Hsu Fang, Chang Po-Rong, and Chan Kuan-Kin (1993), “Optimization of two-dimensional radome boresight error performance using simulated annealing technique,” *IEEE Trans. Antennas Propag.*, Vol.41, No.9, pp.1195-1203,.
- Hsu Fang, Chan Kuan-Kin, Chang Po-Rong, and Chao S. H. (1994), “Optimal boresight error design of radomes of revolving symmetry”, *Electron. Lett.*, Vol.30, No.19, pp.1561-1562.
- Han D. H., Polycarpou A. C., and Balanis C. A. (2002), Hybrid analysis of reflector antennas including higher order interactions and blockage effects, *IEEE Trans Antennas Propagat* 50, 1514-1524.
- Ishimaru A. (1991), *Electromagnetic wave propagation, radiation, and scattering*, (NJ: Prentice Hall, Englewood Cliffs, , pp.31-76.
- Ip H. P. and Yahya Rahmat-Samii (1998), Analysis and characterization of multilayered reflector antennas: Rain/Snow accumulation and deployable membrane, *IEEE Transactions on Antenna and Propagation*, 46(11), 1593-1605.

- Jin J. M. (1993), *The finite element method in electromagnetics*, New York, Wiley.
- Kozakoff D. J. (1997), *Analysis of radome-enclosed antennas*, (Artech House, Boston London).
- Kong J. A. (1986), *Electromagnetic wave theory*, (Wiley-Interscience, New York).
- Lu C. C. (2003), A fast algorithm based on volume integral equation for analysis of arbitrarily shaped dielectric radomes, *IEEE Transactions on Antennas and Propagation*, 51(3), 606-612.
- Mark J. Povinelli and John D'Angelo (1991), Finite element analysis of large wavelength antenna radome problems for leading edge and radar phased arrays, *IEEE Transactions on Magnetics*, 27(5), 4299-4302.
- Meng H. F. Dou W. B. and Yin K. (2008a), Analysis of Antenna-Radome System at Millimeter Wave Band, 2008 Global Symposium on Millimeter Waves Proceeding, GSMM 2008, pp.380-383.
- Meng H. F. and Dou W. B. (2008b), Multi-objective optimization of radome performance with the structure of local uniform thickness, *IEICE Electronics Express*, Vol.5, No.20, pp.882-887.
- Meng H. F., Dou W. B., Chen T. T. and Yin K. (2009a), Analysis of radome using aperture integration-surface integration method with modified transmission coefficient. *Journal of Infrared Millimeter and Terahertz Waves*, Vol.30, No.2, pp.199-210.
- Meng H. F. and Dou W. B. (2009b), Hybrid IPO-BI-FEM for the analysis of 2D large radome with complex structure, *Microwave and Optical Technology Letters*, Vol.51, No.5, pp.1348-1353.
- Nair R. U. and Jha R. M. (2007), "Novel A-sandwich radome design for airborne applications", *Electron. Lett.*, Vol.43, No.15, pp. 787-788.
- Paris D. (1970), Computer-aided radome analysis, *IEEE Transactions on Antennas and Propagation*, 18(1), 7-15.
- Rudge A. W. et al. (1983), *The handbook of antenna design*, (Peter Pergrinus Ltd., London,), Vol.2 pp. 457-553.
- Tricoles G. (1963), Radiation patterns of a microwave antenna enclosed by a hollow dielectric wedge, *Journal of Optical Society of America*, 53(5), 545-557.
- Tzoulis A. and Eibert T. F. (2005), A hybrid FE-BI-MLFMM-UTD method for numerical solutions of electromagnetic problems including arbitrarily shaped and electrically large objects, *IEEE Trans Antennas Propagat* 53), 3358-3366.
- Volakis John L. and Shiflett James A. (1997), CADDRAD: A physical optics radar/radome analysis code for arbitrary 3D geometries, *IEEE Antennas and Propagation Magazine*, 39(6), 73-79.
- Wu D. C. F. and Rudduck R. C. (1974), Plane wave spectrum-surface integration technique for radome analysis, *IEEE Transactions on Antenna and Propagation*, 22(3), 497-500.
- Weile D. S. and Michielssen E. (1997), "Genetic algorithm optimization applied to electromagnetics: a review", *IEEE Trans. Antennas Propag.*, Vol.45, No.3, pp.343-353.
- Walter D. Burnside and Ken W. Burgener (1983), High Frequency Scattering by a thin lossless dielectric slab, *IEEE Transactions on Antenna and Propagation*, 31(1), 104-110.

IntechOpen

IntechOpen



**Microwave and Millimeter Wave Technologies from Photonic Bandgap Devices to Antenna and Applications**

Edited by Igor Minin

ISBN 978-953-7619-66-4

Hard cover, 468 pages

**Publisher** InTech

**Published online** 01, March, 2010

**Published in print edition** March, 2010

The book deals with modern developments in microwave and millimeter wave technologies, presenting a wide selection of different topics within this interesting area. From a description of the evolution of technological processes for the design of passive functions in millimetre-wave frequency range, to different applications and different materials evaluation, the book offers an extensive view of the current trends in the field. Hopefully the book will attract more interest in microwave and millimeter wave technologies and simulate new ideas on this fascinating subject.

**How to reference**

In order to correctly reference this scholarly work, feel free to copy and paste the following:

Hongfu Meng and Wenbin Dou (2010). Analysis and Design of Radome in Millimeter Wave Band, Microwave and Millimeter Wave Technologies from Photonic Bandgap Devices to Antenna and Applications, Igor Minin (Ed.), ISBN: 978-953-7619-66-4, InTech, Available from: <http://www.intechopen.com/books/microwave-and-millimeter-wave-technologies-from-photonic-bandgap-devices-to-antenna-and-applications/analysis-and-design-of-radome-in-millimeter-wave-band>

**INTECH**

open science | open minds

**InTech Europe**

University Campus STeP Ri  
Slavka Krautzeka 83/A  
51000 Rijeka, Croatia  
Phone: +385 (51) 770 447  
Fax: +385 (51) 686 166  
[www.intechopen.com](http://www.intechopen.com)

**InTech China**

Unit 405, Office Block, Hotel Equatorial Shanghai  
No.65, Yan An Road (West), Shanghai, 200040, China  
中国上海市延安西路65号上海国际贵都大饭店办公楼405单元  
Phone: +86-21-62489820  
Fax: +86-21-62489821

© 2010 The Author(s). Licensee IntechOpen. This chapter is distributed under the terms of the [Creative Commons Attribution-NonCommercial-ShareAlike-3.0 License](#), which permits use, distribution and reproduction for non-commercial purposes, provided the original is properly cited and derivative works building on this content are distributed under the same license.

IntechOpen

IntechOpen